Molecular Pharmacology Fast Forward. Published on December 5, 2021 as DOI: 10.1124/molpharm.121.000413
This article has not been copyedited and formatted. The final version may differ from this version.

Thermal unfolding of the human serotonin transporter: differential effect by stabilizing and destabilizing mutations and cholesterol on thermodynamic and kinetic stability

Markus Ponleitner, Daniel Szöllősi*, Ali El-Kasaby, Florian Koban, Michael Freissmuth* and *Thomas Stockner*

Institute of Pharmacology and the Gaston H. Glock Research Laboratories for Exploratory Drug Development, Center of Physiology and Pharmacology, Medical University of Vienna, Austria

Running title: Thermal unfolding of the human serotonin transporter

author for correspondence:

Michael Freissmuth

Institute of Pharmacology and the Gaston H. Glock Research Laboratories for Exploratory Drug Development, Center of Physiology and Pharmacology, Medical University of Vienna, Vienna, Waehringerstrasse 13a, Vienna, 1090 Austria.

Ph.: +43-1-40160 31371

Fax: +43-1-40160 931300

email: michael.freissmuth@meduniwien.ac.at

Number of text pages: 38

Number of Tables: 0

Number of Figures: 8

Number of references: 63

Abstract word count: 232

Introduction word count: 642

Discussion word count: 1495

Abbreviations:

DAT, dopamine transporter; EL, extracellular loop; ER, endoplasmic reticulum; GABA-transporter-1; GABA-transporter-1; IL, intracellular loop; MBCD, methyl-β-cyclodextrin; MD, moleculardynamics; POPC, 1-palmitoyl-2-oleoyl-sn-glycero-3-phosphocholine; SERT, serotonin transporter; SERT-TS2 and -TS3, variants thermostabilized by two or three point mutations, respectively; SLC6, solute carrier 6; TM, transmembrane segment

Abstract

Folding-deficient mutants of SLC6 (solute carrier 6) family members have been linked to human diseases. The serotonin transporter (SERT/SLC6A4) is an important drug target in the treatment of depression, anxiety and obsessive-compulsive disorders and - with structural information in several conformational states - one of the best understood transporters. Here, we surmised that thermal unfolding offered a glimpse on the folding energy landscape of SLC6 transporters. We carried out molecular dynamic (MD) simulations to understand the mechanistic basis for enhanced and reduced stability, respectively, of the thermostabilized variant SERT-Y110A/I291A/T439S, which had previously been used for crystallization of human SERT in the outward-facing state, and of the folding-deficient SERT-P601A/G602A. We also examined the hydrophobic mismatch caused by the absence of cholesterol to explore the contribution of cholesterol to protein stability. When compared to wild type SERT, the thermodynamic and kinetic stability of SERT-Y110A/I291A/T439S was enhanced. In the other instances, changes in these two components were not correlated: the mutations in SERT-P601A/G602A led to a drop in thermodynamic but an increase in kinetic stability. The divergence was even more pronounced after cholesterol depletion, which reduced thermodynamic stability but increased the kinetic stability of wild type SERT to a level comparable to that of SERT-Y110A/I291A/T439S. We conclude that the low cholesterol content of the endoplasmic reticulum facilitates progression of the folding trajectory by reducing the energy difference between folding intermediates and the native state.

Significance statement:

Point mutations in solute carrier 6 (SLC6) family members cause folding diseases. The serotonin transporter (SERT/SLC6A4) is a target for antidepressants and the best understood SLC6. We carried out molecular dynamics simulations and examined thermal unfolding of wild type and mutant SERT variants to understand their folding energy landscape. In the

folding-deficient SERT-P012A/G602A, changes in kinetic and thermodynamic stability were not correlated. Similarly, cholesterol depletion lowered thermodynamic but enhanced kinetic stability. Our observations allow for rationalizing the action of pharmacochaperones.

Molecular Pharmacology Fast Forward. Published on December 5, 2021 as DOI: 10.1124/molpharm.121.000413
This article has not been copyedited and formatted. The final version may differ from this version.

Introduction

With more than 400 members, the solute carrier family is the second largest membrane protein family in the human genome (Perland and Fredriksson, 2017). The genetic variation in SLC transporters is large and more than 100 SLC transporters have been linked to a human disease (Schaller and Lauschke, 2019). In the past 20 years, there has been a steady increase in the number of point mutations of SLC transporters, which give rise to folding-deficient proteins (Bhat et al., 2021a). Based on the number of publications, the serotonin transporter (SERT, SLC6A4) can be argued to be the most extensively studied transporter (César-Razquin et al., 2015): it has a rich pharmacology (Sitte and Freissmuth, 2015), which comprises both typical and atypical inhibitors, partial and full releasers (Bhat et al, 2019; Hasenhuetl et al., 2019), its structure has been solved in several conformations (Coleman et al., 2016, Coleman and Gouaux, 2018; Coleman et al., 2019) and its transport cycle has been analyzed with high precision (Schicker et al., 2012; Hasenhuetl et al., 2016; Bhat et al., 2021b).

The folding trajectory of SLC transporters is of interest, because folding-deficient mutants are amenable to rescue by pharmacochaperoning (El-Kasaby et al., 2010; Koban et al., 2015; Kasture et al., 2016; Beerepoot et al., 2016; Asjad et al., 2017; Bhat et al., 2017; Bhat et al., 2021c) or by interfering with the endogenous proteinaceous chaperones (Fujiwara et al., 2013; El-Kasaby et al., 2014 & 2020). Conceptually, the action of pharmacochaperones can be accounted for by four mechanisms of action (Marinko et al., 2019): binding to and stabilization of the (i) native (=folded) state or (ii) folding intermediate(s); (iii) suppression of aggregate formation; (iii) dissolution of aggregates. In the vast majority of cases, the pharmacochaperoning action is thought to arise from the first mechanism, i.e. thermodynamic stabilization of the native state (Marinko et al., 2019). Circumstantial evidence, however, suggests that pharmacochaperones may rescue folding-deficient variants of SERT and of the

dopamine transporter (DAT, SLC6A3) by an action on (a) folding intermediate(s) (Bhat et al., 2021c). Progress is hampered by the elusive nature of the folding intermediates. The folding trajectory can be conceptualized as a conformational search, where the protein moves through a funnel-like energy landscape to reach a minimum energy conformation (Dill and Chan, 1997). However, the surface of this landscape is rugged, i.e. energy barriers must be overcome during the folding trajectory (Hartl et al., 2011). Mutations increase the propensity for trapping of folding intermediates; these traps can be overcome by pharmacochaperones (Freissmuth et al., 2017). In addition, the native state is not necessarily the minimum energy conformation (Hartl et al., 2011). In fact, because SLC transporters operate by an alternating access mechanism, the transporter has to visit several distinct conformations during the transport cycle, most importantly the outward, occluded and inward facing states. Hence, the required conformational flexibility imposes an additional limit on the shape of the energy landscape. Here we surmised that thermal unfolding of SERT provided information on the barriers, which separated the folded from unfolded states. We compared wild type human SERT to a thermostabilized version of human SERT, which was instrumental for crystallization of the protein (SERT-Y110A/I291A/T439S = SERT-TS3; Coleman et al., 2016), a folding-deficient version, which is amenable to rescue by pharmacochaperoning (SERT-P601A/G602A; El-Kasaby et al., 2014) and a version, in which one cholesterol binding site was disrupted (Laursen et al., 2018). MD simulations allowed for rationalizing, how the mutations and the membrane lipids affected the stability of the protein. Our observations show that two components - i.e. a kinetic and a thermodynamic component - contribute to the stability of SERT. These were differentially affected by the mutations and by cholesterol depletion. To the best of our knowledge, the current approach is the first to combine thermal inactivation of a membrane protein with MD simulations to extract information relevant to the folding problem.

Materials and Methods:

Materials

Cell culture media and G418/geneticine were purchased from SigmaAldrich and Biochrom, respectively. [^{3}H]Imipramine (51.6 Ci/mmol and 40.0 Ci/mmol) was from PerkinElmer and unlabeled paroxetine from Santa Cruz Biotechnology. Methyl-β-cyclodextrin (MβCD) and all other reagents were obtained from SigmaAldrich and were of analytical grade. Mutations were introduced into the plasmid containing the N-terminally-YFP-tagged, full-length human serotonin transporter (SERT) using the QuikChange-Lightning kit for site directed mutagenesis from Agilent Technologies to obtain the SERT-V367N, SERT-TS_2^*(SERT-I291A/T439S) and -TS_3^*(SERT-Y110A/I291A/T439S) mutants after serial mutagenesis. We denote the variants TS_2^* and TS_3^*, which were employed in this study, by asterisk to indicate the full-length protein containing the specified mutations, as opposed to the crystallized and N- and C-terminally truncated SERT-TS2 and SERT-TS3 (Coleman et al., 2016). The presence of the mutation(s) was verified by sequencing the entire reading frame of each construct.

Cell culture and membrane preparation

HEK293 cells were stably transfected with plasmids encoding YFP-tagged wild type SERT, SERT-TS_2^*, SERT-TS_3^*, SERT-V^{367}N and the folding-deficient SERT-P601A/G602A. Cells expressing SERT-P601A/G602A were incubated for 24h in the presence of 30 µM noribogaine to correct the folding defect by pharmacochaperoning (El-Kasaby et al., 2014). Confluent monolayers of cells were mechanically detached and lysed in hypotonic buffer (20 mM Hepes.NaOH, pH 7.4, 1 mM EDTA, 2 mM $MgCl_2$). The cell suspension was frozen in liquid nitrogen, subjected to freeze-thaw cycles and sonicated. The homogenate was finally centrifuged at 30,000 g for 30 min at 4°C. The pellet was resuspended in buffer at a protein concentration of about 2 mg/ml. Membranes were depleted of cholesterol by incubation in the

presence of methyl-β-cyclodextrin (final concentration of 10 mg/mL) for 30 min incubation at 37°C with gentle shaking (Scanlon et al., 2001). Thereafter the membranes were harvested by centrifugation at 16,000 g for 15 min, the methyl-β-cyclodextrin containing supernatant was removed and, after one additional washing step, the pellet was resuspended in buffer.

Thermal inactivation and radioligand binding

Temperature-induced inactivation was determined by incubating duplicate samples (containing 5-40 µg protein) in buffer containing (120 mM NaCl, 20 mM Tris.HCl, 3 mM KCl, 2 mM $MgCl_2$, 1 mM EDTA, pH 7.4) for 15 min at temperatures ranging from 43°C to 78°C. In some instances, NaCl was replaced by equimolar choline chloride. Thereafter the samples were put on ice. For time-dependent denaturation, duplicate samples (containing 5-40 µg of protein per sample) were incubated at the indicated temperature for time intervals ranging from 0 to 80 minutes and subsequently put on ice.

After thermal inactivation, the amount of residual, functional SERT was determined by incubating the membranes on ice for 15 min in a final volume of 0.2 ml buffer (120 mM NaCl, 20 mM Tris-HCl, 3 mM KCl, 2 mM $MgCl_2$, 1 mM EDTA, pH 7.4) in the presence of [^{3}H]imipramine (3 nM, 6nM for SERT-V^{367}N). Nonspecific binding was defined in parallel incubations in the presence of 10 µM paroxetine. Preliminary experiments verified that binding equilibrium was reached rapidly (i.e. within 5 min) on ice (data not shown). The reaction was terminated by rapid filtration through glass-fiber filters precoated in 1% PEI (polyethyleneimine) with ice-cold buffer (120 mM NaCl, 10 mM Tris-HCl, 1 mM Mg^{2+}, pH 7.4). The radioactivity retained on the filters was determined by liquid scintillation counting.

Molecular dynamics simulations

For the molecular dynamics (MD) simulations the outward open human SERT crystal structure was used (PDB ID: 5I71; Coleman et al., 2016). Missing side chains and bound ions

were positioned using MODELLER 9.20 (Shen et al., 2006; Webb and Sali, 2014) creating 100 structures from which the best 5 were selected based on the DOPE score. The resulting structures where then mutated by replacing P601 and G602 to alanine using Pymol, v1.8.4 (The PyMOL Molecular Graphics System, version v1.8.4 Schrödinger, LLC). All proteins contained 2 Na^+ ions and a Cl^- ion at their respective binding sites. All models were converted into coarse grain representation using the MARTINI force field (Monticelli et al., 2008; de Jong et al. 2013; Wassenaar et al., 2015) and embedded into a POPC:cholesterol membrane (70:30 mol%) to obtain an equilibrated membrane lipid environment. The simulation box was filled with water and 150 mM NaCl. The coarse grain systems were simulated for 1 μs with the protein structure restrained to avoid conformational changes while equilibrating the lipid membrane. For wild type protein POPC only membranes were also prepared. Membrane lipids, water and ions of the equilibrated coarse grain systems were converted to an all-atom representation (Wassenaar et al., 2014). The original protein models were inserted into the membrane using the *membed* procedure (Wolf et al., 2010) to relax possible local atom overlaps. Protein, ions and solvent were described using the amber99sb-ildn force field (Lindorff-Larsen et al., 2010), POPC and cholesterol by Slipid (Jämbeck and Lyubartsev, 2012; 2013).

All simulations used GROMACS version 2018.1 (Abraham et al., 2015). The final assembled systems were energy-minimized and equilibrated in four steps of 2.5 ns each by slowly releasing the position restrains (1000, 100, 10, 1 kJ/mol/nm) active on the Cα atoms and bound ions. The production runs were carried for 500 ns, each system independently simulated five times without applying restraints. Temperature was maintained at 310 K using the v-rescale (τ = 0.5 ps) thermostat (Bussi et al., 2007), while separately coupling protein, membrane and solvent. Pressure was maintained at 1 bar using the Parrinello-Rahman barostat (Parinello and Rahman, 1981) in a semiisotropic manner and applied a coupling constant of 20.1 ps. Long range electrostatic interactions were described using the smooth

particle mesh Ewald method (Darden et al., 1993) applying a cutoff of 0.9 nm. The van der Waals interactions were described using the Lennard Jones potentials applying a cutoff of 0.9 nm. Long range correction for energy and pressure were applied. Coordinates of all atoms were recorded at every 10 ps.

Biased simulations

Equilibrated systems of wild type SERT and SERT-P601A/G602A were tested using well-tempered metadynamics (WTM, Barducci et al., 2008). The technique allows for fast exploration of the free energy landscape, while limiting the search to low energy conformations. Exploration is promoted by the local addition of small Gaussian shaped potentials, which eventually fill the complete free energy landscape resulting in a flat free energy hypersurface. Inversion of the total added potential equals the free energy. WTM was performed by simultaneous use of GROMACS and Plumed (Tribello et al., 2014; The Plumed consortium, 2019). Biased simulations were 200 ns long in 5 parallel runs. The C-terminal helix unfolded irreversibly in one trajectory, which was discarded from further analysis. Reweighting of the WTM trajectories (Tiwary and Parrinello, 2015; Lindahl et al., 2017) was use to query the free energy landscape along non-biased degrees of freedom. We used the distances between P156-S611 and L597-R607, which gives a better description of motions of the C-terminus (cf. Fig. 3D). Moreover, reweighting also allows for merging results of parallel simulations providing a complete free energy estimation of the sampled conformational space.

Statistics

The study was exploratory in nature. Accordingly, the number of independent experiments (n= 3 to 5) was chosen to verify the reproducibility of the data and there weren't any preplan-ned statistical tests. Data obtained by temperature-dependent inactivation of wild type and

mutant versions SERT were fitted by curvilinear regression to a three-parameter logistic equation $B_{(T)} = \frac{B_0 \cdot T^p}{TM_{50}^p + T^p}$, where $B_{(T)}$ is binding at temperature T, B_0 is control binding in the absence of thermal denaturation (i.e. at 22°C), TM_{50} is the temperature resulting in 50% inactivation and p is the slope of the curve. Data obtained by time-dependent inactivation at fixed temperatures were fitted by curvilinear regression to the equation for a mono- ($B_{(t)} = B_0 \cdot e^{-k \cdot t}$) or biexponential decay ($B_{(t)} = B1 \cdot e^{-k1 \cdot t} + B2 \cdot e^{-k2 \cdot t}$), where $B(t)$ is binding observed at time t; k, $k1$ and $k2$ are the rate constants for thermal inactivation by a monophasic inactivation and for rapid and slow thermal inactivation, respectively; $B1$ and $B2$ are the fraction of control binding B_0 undergoing rapid and slow thermal inactivation, respectively. We used an F-test based on the extra-sum-of-squares to verify that the more complex model improved the fit in a statistically significant manner: $F = \frac{\frac{SS_{ME} - SS_{DE}}{DF_{ME} - DF_{DE}}}{\frac{SS_{ME}}{DF_{ME}}}$, where SS_{ME} and SS_{DE} are the sum of squares of the deviation from the fitted lines for the mono- and the double-exponential decay, respectively; DF_{ME} and DF_{DE} are the corresponding degrees of freedom (i.e. the number of data points minus the number of parameters in each equation).

Results

Thermostability of SERT variants in the lipid bilayer:

The thermostability of SERT and of mutated variants was previously determined in detergent solution (Green et al., 2015). Here we assessed the thermostability of SERT in membranes. We first verified that [^{3}H]imipramine bound to SERT, if the membranes were incubated on ice. This was the case: the binding equilibrium was rapidly reached (k_{app} = 0.54 min^{-1} at 3 nM radioligand concentration); binding remained stable for at least 60 min (data not shown). Hence, in all experiments, samples were subjected to heat denaturation for defined time intervals at the specified temperature and the remaining active (i.e. binding competent) SERT was subsequently determined by binding of [^{3}H]imipramine at 0°C. We first compared the

temperature stability of wild type SERT with the two thermostable variants identified by Green et al. (2015), namely SERT-TS2* (=SERT-I291A/T439S) and SERT-TS3* (SERT-Y110A/I291A/T439S). When incubated for 15 min, wild type SERT was remarkably stable: temperatures exceeding 55°C were required to cause loss of binding (full circles in Fig. 1). As expected, the denaturation curved of the heat-stable mutants SERT-TS_2^* (triangles in Fig. 1) and SERT-TS_3* (squares in Fig. 1) were shifted to the right. In addition, we also examined SERT-P601A/G602A; this mutation, which is in the loop connecting the TM12 with the C-terminal α-helix (cf. Fig. 3), results in misfolding and ER retention of SERT (El-Kasaby et al., 2010) but the folding deficit can be corrected by pharmacochaperoning with noribogaine (El-Kasaby et al., 2014). Accordingly, we incubated cells expressing SERT-P601A/G602A for 24 h in the presence of noribogaine prior to membrane preparation. This restored surface levels of active transporter to about 10 to 15% of those seen in cells expressing wild type SERT (Bhat et al., 2020). If membranes harboring rescued SERT-P601A/G602A were exposed to increasing temperature (triangles in Fig. 1), the protein substantially was more temperature-sensitive than the wild type transporter. T_M, the temperature required for inactivating 50% of SERT, was 60.5 ± 0.5, 63.8 ± 1.0, 68.5 ± 0.5, 49.4 ± 0.5°C (mean ± S.D; n≥3) for wild type SERT, SERT-TS_2*, SERT-TS_3* and SERT-P601A/G602A, respectively. Thus, when compared to the earlier observations (Green et al., 2015), it is evident that membrane-embedded SERT is substantially more resistant to heat denaturation than the transporter in detergent micelles: the shift in T_M by about 20°C is pronounced for wild type SERT, but it is still substantial for the thermostable mutants, e.g. for SERT-TS_3^* the difference in T_M between membrane-bound and detergent-solubilized state is about 9°C. We carried out the heat-inactivation in the presence of 120 mM Na^+. Sodium stabilizes the outward-facing conformation. In the absence of sodium, the inward-facing state is favored. However, replacing sodium by equimolar choline did not produce any appreciable shift in the thermal inactivation curve of wild type SERT (T_M = 60.7 ± 0.4°C; open circles in Fig. 1).

Molecular Pharmacology Fast Forward. Published on December 5, 2021 as DOI: 10.1124/molpharm.121.000413
This article has not been copyedited and formatted. The final version may differ from this version.

Calculation of structural stability

Binding of typical inhibitors (including radioligands such as [^{3}H]imipramine and [^{3}H]paroxetine) requires SERT to reside in the outward-facing conformation. SERT-TS3 has been crystallized in the outward-facing state and was shown to be binding competent but transport-deficient (Green et al., 2015). SERT-TS3 is locked in the outward-facing state and fails to undergo the conformational transitions required to support a transport cycle. This phenotype is consistent with the implicit assumption that the three mutations in SERT-TS3 (SERT-Y110A/I291A/T439S) privilege the outward-facing conformation over all other conformations. The increased stability is expected to be detectable by an increased rigidity. We examined this conjecture by carrying out comparative molecular dynamics simulations of wild type SERT and SERT-TS3 with the proteins embedded in a lipid bilayer. These simulations reveal distinct local structural and/or dynamic effects for each of the three mutations (Y110A, I291A and T439S, illustrated in Fig. 2A) that contribute to structural stabilization (Fig. 2). The mutations lead to a small global change of fluctuations in SERT-TS3 (Fig. 2B). In addition, the conformation of the bundle domain is less open, as TM1b moves toward a more occluded geometry (Fig. 2C and D). The mutation of Y110A changes a large amino acid (tyrosine) to a small amino acid (alanine). The side chain of Y110 is buried between TM1, TM7, TM8, EL3 and EL4 (Fig. 2C). The alanine mutant leaves empty space, which is filled by a closer packing of these helices and loops (Fig. 2E) and by the movement of TM1b (Fig. 2C).

Similarly, the I291A mutation introduces a smaller amino acid, which is located in the interface between TM5 and TM8 (Fig. 2F). Conceptually, this reduction in size of the side chain at position 291 creates a local void that leads to a closer association of TM5 and TM8 (Fig. 2G). This displacement fills a large part of the empty volume created by the mutation

but residual sub-atom size cavities remain detectable (Fig. 2F). In addition, the rearrangement also translates into a compression of the helix-helix interface of the preceding and following helical turn. Thus, the structural and dynamic changes in the vicinity of A291 stabilize the TM5-TM8 interface through tighter association. It is conceivable that this suppresses the propensity of SERT-TS3* to visit conformations, which allow for transition to the unfolded state(s). Most prominently, the dynamics of the juxtaposed residue I426 are increased by the I291A mutation visible as an altered dihedral distribution (Fig. 2H). This leads to an increase in local conformational entropy (wild type SERT: -24.9±2.2 kJ/mol; SERT-TS3: -21.6±2.2 kJ/mol relative to the unfolded state, obtained using PDB2entropy; Fogolari et al., 2018). The effect of the third mutation (T439S) on SERT stability can be accounted for by two effects:(i) removal of the β-branched methyl-group of threonine changes the side chain conformation, which alters the hydrogen bonding pattern of the side chain hydroxyl group. The TM8 destabilizing hydrogen bond between the side chain of residue 439 and the backbone carbonyl oxygen of G435 (Fig. 2I and K) is replaced by the interaction with the buried side chain of N177 (Fig. 2J and L). Both, the loss of the interaction between G435 and T439 and the newly acquired H-bond to N177 in SERT-TS3 contribute to stabilizing the outward-open conformation due to the absence of a helix destabilizing effect and the presence of a helix interconnecting interaction. (ii) In addition, the reorientation of the side chain of residue 439 leads to a stabilization by strong interactions of a structural water molecule between TM3 and TM8 (Fig. 2J). In wild type SERT, the position of this water molecule is diffuse (Fig. 2I), because it lacks the stabilizing interaction, which is only established after the rotation of the hydroxyl group of S439 in SERT-TS3. Taken together, both, the mutations Y110A and I291A introduce a much smaller residue, leading to potential voids. These residue changes lead to a local compacting of SERT-TS3. These changes therefore are predicted to raise ΔG^* for unfolding (i.e. the energy barrier separating the folded from the unfolded states), because they increase the interaction enthalpy of the tightly packed residues around the mutation sites.

Concomitantly, ΔG for unfolding (i.e. the free energy difference between the folded and the unfolded states) declines, because the entropy of the closely associated residues is increased. Accordingly, upon unfolding, the free energy gain in entropy is smaller. The T439S mutant changes the hydrogen bonding pattern and thus contributes to stabilizing TM8 and to strengthening the interaction with a structural water molecule.

We carried out similar calculations for SERT-P601A/G602A (Fig. 3). RMSF calculations provide evidence for structural instability: in SERT-P601A/G602A, the N-terminal half of TM5 and the segment of the C-terminus adjacent to TM12 are much more dynamic and visited several new conformations not sampled by wild type SERT (Fig. 3B). Based on these fluctuations observed in the C-terminus (Fig. 3B), we surmised that the destabilizing effect of the P601A/G602A mutation arose - at least in part - from an altered interaction of the C-terminal helix with the protein core. We explored this hypothesis in biased simulations to assess how strongly the C-terminus is attached to the rest of the protein using well-tempered metadynamics (Barducci et al., 2008). The method enhances the sampling along a pre-selected reaction coordinate, which in this case was the distance between TM12 and the C-terminal helix (backbone center of mass of residue 576-584 versus 607-613, Fig. 3A). The bias translates to pulling the C-terminal helix parallel to the z-axis, i.e. away from the core of SERT. Then, using a reweighting technique the observed changes can be translated to a free energy landscape in relation to the distances between P156 – S611 and L597 – R607 (Fig. 3D). The P156 – S611 distance captures the attachment of the helix to the protein core, while L597 – R607 describes changes in the geometry of the loop between TM12 and the C-terminus. It is evident that the P601A/G602A mutation lowers the energy barrier to visit other, more open conformational states (Fig. 3D), which is a signature of a decreased overall resistance against unfolding.

Two components in the heat-induced inactivation of wild type and mutant SERT variants

Assuming that a possible unfolding route is initiated by the detachment of the C-terminus, the results summarized in Fig. 3 are consistent with the lower thermostability of SERT-P601A/G602A (Fig. 1). However, it is only possible to obtain relative comparisons, if proteins are subjected to heat inactivation for an arbitrarily selected time (15 min in the experiment in Fig. 1). More information can be extracted by observing the time-dependent denaturation. This allows for estimating the two components of protein stability, i.e. thermodynamic stability and kinetic stability (Sanchez-Ruiz, 2010): kinetic stability results from an energy barrier (ΔG*), which prevents the native state from visiting (partially) unfolded states. Thermodynamic stability is imparted by the lower energy content of the native folded conformations than of the unfolded states. These two population states are not separated by a high energy barrier and hence can rapidly equilibrate. If thermodynamic stability is high at a given temperature, the Gibbs free energy favors the native state at equilibrium and thus conformations conducive to unfolding are rarely populated. Accordingly, we explored, which component of protein stability was affected by the mutations by incubating membranes harboring wild type SERT (Fig. 4A), SERT-TS3* (Fig. 4B) and SERT-PG601,602-AA (Fig. 4C) for different time intervals at temperatures close to their individual melting temperatures, i.e. T_M –5°C, T_M –3°C, T_M, T_M +3°C (T_M rounded to integers). When subjected to this thermal challenge, all SERT variants underwent two distinct phases of denaturation provided that the temperature did not exceed T_M by 3°C: a rapid decrease of [^{3}H]imipramine binding was followed by a slower component (Fig. 4). With the notable exception of curves generated at the highest temperature (i.e., T_M +3°C), the data were better described by the equation for double exponential than for a mono-exponential decay. The rate of the slow component increased with higher temperatures. Accordingly, it was possible to estimate the energy barrier, which separated the folded from the binding-

incompetent, unfolded state(s), from the corresponding Arrhenius plots: it is evident from Fig 5A that their slopes differ. Slow thermal inactivation required a substantially higher activation energy in SERT-TS3* (303 kJ·mol^{-1}) than in wild type SERT (113 kJ·mol^{-1}) or SERT-P601A/G602A (176 kJ·mol^{-1}). In contrast, the fast component of thermal inactivation did not increase to any appreciable extent with increasing temperature: this is most readily evident for SERT-P601A/G602A (cf. full squares in Fig. 5B). We stress that in wild type SERT (closed circles in Fig. 5B) and SERT-T3* (open triangles in Fig. 5B), the fraction, which denatured rapidly at T_M– 5°C, T_M–3°C was too small to obtain a reliable estimate of the rate. Taken together, the observations summarized in Fig. 5A&B are consistent with the interpretation that the fast and the slow component of thermal inactivation reflect the thermodynamic and the kinetic stability, respectively, of wild type and mutant SERT variants.

We extracted the ratios of the slowly denaturing component over the rapidly unfolding component (P_f/P_u) from the biexponential decay curves shown in Fig. 5 and plotted these as a function of temperature (1/K) (Fig. 5C). This allows for estimating the thermodynamic stability of the SERT variants from the x-axis intercept. The thus calculated T_M-values (60.3°C, 70.8°C and 48.1°C for wild type SERT, SERT-TS3* and SERT-P601A/G602A, respectively) were in reasonable agreement with the estimates obtained from Fig. 1. This was to be expected, because the slow component only contributed to a minor extent to thermal inactivation within the first 15 min.

Contribution of cholesterol to SERT stability

Regardless of whether only the component of thermodynamic stability (Fig. 5C) or the global T_M (measured at 15 min, Fig. 1) is taken into account, the melting temperature estimates are higher by >10° than those in detergent solution (Green et al., 2015). The difference indicates that the membrane lipids have a strong stabilizing effect. Cholesterol has been visualized in

the crystal structure of SERT (Coleman et al. 2016); this is also true for the closely related dopamine transporter/DAT, albeit wedged to the hydrophobic core at a different position (Penmatsa et al., 2013). SERT requires cholesterol for its eponymous action, i.e. serotonin transport (Scanlon et al., 2001), and apparently cannot fold correctly in the absence of cholesterol (Tate et al., 2003). We therefore surmised that cholesterol affected the stability of SERT. Accordingly, we carried out MD simulations with SERT embedded in lipid bilayers containing solely POPC or the combination of POPC and cholesterol (molar ratio 70:30). We first analyzed the thickness of the membrane around the protein by measuring the distance between the phosphate atoms of the POPC head groups in the inner and outer leaflet (Fig. 6A). The average thickness clearly shows that the membrane containing POPC and cholesterol matches the hydrophobic core of SERT (Fig. 6B). In contrast, a bilayer comprised solely of POPC is too thin (Fig. 6B and D). However, it is also visible that the presence of SERT increases the local thickness. The thickness maps (Fig. 6C&D) also indicate that the hydrophobic core of SERT exerts different, non-homogeneously distributed forces on the surrounding lipids: in contrast to helix 11, which produces a bulge in the bilayer (seen as prominent yellow area highlighted by a magenta arrow in Fig. 6D), on the opposite side, the lipid exposed surface in the vicinity of helix 5 allows for membrane thinning (seen as blue area highlighted by an orange arrow in Fig. 6C). The same is true in the vicinity of helix 2 (seen again as blue area highlighted by a black arrow in Fig. 6C).

Taken together, these observations suggest that the annular lipid ring surrounding SERT differs in the absence and presence of cholesterol. Without cholesterol, the reduced thickness results in a hydrophobic mismatch, which is predicted to translate into a gain of entropy in both the bilayer and the protein. Accordingly, we explored the consequence of removing cholesterol in comparative molecular dynamics simulations of wild type SERT embedded in a lipid bilayer containing or lacking cholesterol. This analysis revealed that the overall

differences in the fluctuations of the backbone (Cα) were modest (Fig. 7A and C): in the hydrophobic core, they were confined to the bottom of helix 8 and the top of helix 11, which increased in the absence of cholesterol. The fluctuations in the side chains were also enhanced in these regions, but they were also increased in other hydrophobic segments, e.g. TM4, TM5, TM6 and TM7 (Fig. 7B and D). Interestingly, in the presence of cholesterol, fluctuations of both the backbone (Fig. 7A and C) and the side chains (Fig. 7B and D) were enhanced in EL2 and IL4. This suggests that the absence of cholesterol leads to a gain in entropy in the hydrophobic core but to a drop in entropy in EL2 and IL4.

We verified the effect of cholesterol depletion on the thermostability of SERT by comparing the susceptibility of wild type SERT and on SERT-V367N. This mutation was selected, because it reduces the affinity of cholesterol to one of its *bona fide* binding sites of SERT (Laursen et al., 2018). Thus, it is predicted to be more susceptible to lowering cholesterol levels in the membrane. Membranes harboring wild type SERT and on SERT-V367N were subjected to extraction with methyl-β-cyclodextrin (MBCD, 10 mg/mL) and to a sham procedure. We note that this sham procedure (i.e., incubation of membranes at 37°C followed by centrifugation) *per se* lowered the melting temperature of wild type SERT (T_M = 57.6 ± 0.4°C) by about 3°C (cf. Figs 1 and 8A). However, removal of cholesterol by exposing the membrane to MBCD shifted the melting curve to the left by an additional 4.1°C (T_M = 53.5 ± 0.3°C, full symbols in Fig. 8A). More importantly, SERT-V367N was not only less thermostable (T_M = 54.9 ± 0.3, full symbols in Fig. 9B) than wild type SERT, it was also more affected by cholesterol depletion. The melting curve shifted by about 7°C (T_M = 47.8 ± 0.4, open symbols in Fig. 8B). This finding supports the conclusion that cholesterol is one of the lipids, which define the thermostability of SERT.

Cholesterol depletion has been proposed to reduce the conformational flexibility of SERT (Laursen et al., 2018) and its close relative DAT (Jones et al., 2013) by trapping the proteins in the inward facing conformation. Accordingly, we examined the contribution of thermodynamic and kinetic stability to the shift in thermal denaturation after cholesterol depletion (Fig. 8C) and extracted the rates to generate Arrhenius plots (Fig. 8D). After removal of cholesterol, the rate of slow inactivation of SERT increased steeply with temperature (Fig. 8D): thus, after depletion of cholesterol, the kinetic stability of SERT (357 kJ mol^{-1}) was substantially higher than in native membranes (113 kJ·mol^{-1}; cf. Fig. 5A) and approached that of SERT-TS3*. In contrast, the thermodynamic stability decreased after cholesterol depletion: an x-axis intercept of 52.9°C was calculated from the plot of the fraction of slowly unfolding SERT (Pf/Pu) over the reciprocal of temperature (Fig. 8E) and thus consistent with the T_M determined by the approach used in Fig. 8A.

Molecular Pharmacology Fast Forward. Published on December 5, 2021 as DOI: 10.1124/molpharm.121.000413
This article has not been copyedited and formatted. The final version may differ from this version.

Discussion

Transmembrane transporters operate in a lipid environment and must visit different conformations during their transport cycle. The membrane lipids provide a stabilizing effect by constraining the hydrophobic core but hydrophobic mismatches must be accommodated during the conformational changes. Here, we compared different versions of SERT to explore the mechanisms underlying changes in their stability and to understand the role of cholesterol in supporting the folding and function of the protein. SERT-TS3 is thermostabilized but transport-deficient, because it is trapped in the outward-facing state (Green et al., 2015; Coleman et al., 2016). In contrast, the mutations in SERT-P601A/G602A impair folding of the protein. However, when rescued by pharmacochaperoning, SERT-P601A/G602A translocates substrates and thus is capable of undergoing all conformational transitions required to complete a transport cycle (El-Kasaby et al., 2014; Bhat et al., 2017). The basis for the enhanced and reduced stability of SERT-TS3*-mutant and SERT-P601A/G602A, respectively, can be rationalized from our observations. The MD simulations show that two of the three mutations (i.e. Y110A and I291A) of SERT-TS3 increase the interaction enthalpy and that the third mutation (T439S) provided additional hydrogen bonding. Thus, the mutations were predicted to augment the barrier separating the folded from the unfolded state(s). This prediction was confirmed by determining the time-dependent inactivation of SERT-TS3*: the kinetic stability of the protein was enhanced by about 3-fold when compared to wild type SERT. In addition, the thermodynamic stability was also substantially increased (by about 10°C). This can be attributed to the enhanced overall rigidity of the protein, but the local gains in entropy, which were detected by the MD simulations, also make a substantial contribution. The link between entropy to thermodynamic stability can be rationalized as follows: increased entropy (e.g. introduction of void by smaller residues as in SERT-TS3*) can lead to increased thermal stability, because the ΔS of unfolding (the energetic gain of the system upon unfolding) decreases (Karshikoff et al., 2015). In addition, the presence of voids,

which are too small to be filled by atoms (e.g. water) lead to an increased transition barrier. Similarly, the MD simulations for SERT-P601A/G602A highlighted the mechanistic basis for the reduced stability of the protein: the substitution by two alanine residues does not per se destabilize the amphipathic helix, but allows for many conformations to be visited. Accordingly, the compact structure of SERT, which is supported by a salt bridge between E615 at the end of the amphipathic helix and R152 in intracellular loop 1 (IL1) (Koban et al., 2015), is not maintained. The population of states, where the C-terminal helix is detached by up to 1 nm from the hydrophobic core, offers possible routes for unfolding of the protein. Thus, the MD simulations predicted a reduced thermodynamic stability for SERT-P601A/G602A and this prediction was verified by measuring the time-dependent inactivation of the protein.

The melting temperature of wild type SERT SERT-TS2* and SERT-TS3*, which we observed (i.e., about 61°C, 64°C and 69°C, respectively), were substantially higher than those determined for the solubilized proteins (40°C, 52°C and 59°C, respectively; Green et al., 2015). Our constructs differ from those used by Green et al. (2015) in two aspects: we examined YFP-tagged, full-length versions rather than the C- and N-terminally truncated versions, which were more suitable for X-ray crystallography. These differences are unlikely to confound the analysis. The truncated portion of the N- and C-termini of SERT are thought to contain large unstructured segments (Fenollar-Ferrer et al. 2014). They are hence unlikely to exert a stabilizing effect on the hydrophobic core. Similarly, the N-terminal YFP-tag is unlikely to affect thermal stability; YFP is a stable protein, which can freely float in the cytosol, when connected to the flexible N-terminus (Tsien, 1998). It is unlikely to interact with the hydrophobic core of the transporter. In fact, although extensively examined, an N-terminal YFP-tag has not been found to affect any biochemical activity or partial reaction of SERT. Thus, we conclude that it is the membrane lipids, which account for the large

difference in melting temperature. It is unsurprising that lipids exert a stabilizing effect on SERT. In fact, the melting temperature of the erythrocyte anion exchanger (band 3/SLC4A1) depends on the length of the lipid chains: long chain lipids enhance the stability of the protein, as does cholesterol (Maneri and Low, 1988). Here we focused on cholesterol for several reasons: cholesterol has been visualized in the crystal structures of SERT (Coleman et al., 2016) and - albeit at a different position of drosophila DAT (Penmatsa et al., 2013). MD simulations indicate up to six putative binding sites for cholesterol in SERT (Ferraro et al., 2016). In the absence of cholesterol, SERT cannot be expressed in a functionally active form (Tate et al., 2013). Our MD simulations of SERT revealed a major hydrophobic mismatch in the bilayer lacking cholesterol. The hydrophobic mismatch introduces a penalty in the free energy of the protein. The predicted impact on protein stability was confirmed by examining the effect of cholesterol depletion using two approaches: (i) depletion of cholesterol lowered the thermodynamic stability of wild type SERT. (ii) We examined the thermostability of the SERT-V367N mutant (Laursen et al., 2018). The mutation disrupts one of the candidate cholesterol binding sites (Ferraro et al., 2016; Laursen et al., 2018). As predicted, SERT-V367N was less stable and more susceptible to cholesterol depletion. The transport cycle of SERT-V367N is impaired, because the protein is trapped in the inward-facing conformation (Laursen et al., 2018). Similarly, cholesterol depletion is thought to shift the wild type SERT into the inward-facing state (Laursen et al., 2018). We rule out that this conformational switch *per se* contributes to the reduction in T_M: the thermostability of wild type SERT was comparable in the presence of sodium, which stabilizes the outward-facing conformation, and of choline, which promotes the inward-facing state (Hasenhuetl et al., 2016).

Cholesterol supports the ability of SERT to translocate substrate (Scanlon et al., 2001). This is also true for its close relative DAT (Jones et al., 2012) and the more distantly related GABA-transporter-1 (GAT1/SLC6A1; Shouffani and Kanner, 2000). Cholesterol depletion reduced

the thermodynamic stability but enhanced the kinetic stability. In fact, the kinetic stability of wild type SERT in the absence of cholesterol was comparable to that of the transport-deficient SERT-TS3*. We therefore surmise that the enhanced kinetic stability reflects a drop in conformational flexibility required for supporting the transport cycle. Our MD simulations identified a major difference in fluctuations of EL2 and IL4 in the absence and presence of cholesterol. EL2 moves upward during the transition from the outward- to the inward-facing state (Coleman et al., 2019; Esendir et al., 2021). Thus, it is tempting to speculate that the decrease in transport caused by cholesterol depletion is causally related to the reduction in the mobility of EL2 in the absence of cholesterol.

In its simplest version, the Lumry-Eyring model posits a two-step process for protein unfolding, i.e. N □ U □ D, where N, U and D are the native, reversibly unfolded and irreversibly denatured states, respectively (Lumry and Eyring, 1954). Even brief incubations at elevated temperatures resulted in irreversible loss of binding-competent SERT. Thus, we failed to access the initial transition N □ U, which corresponds to reversible unfolding/refolding. Because of this shortcoming, the energy change ΔG (or ΔH and ΔS), which is associated with the reversible unfolding/refolding reaction, remains inaccessible. However, based on our data, it is nevertheless possible to separate the two components of protein stability, i.e. thermodynamic and kinetic stability, and to infer the energy barriers ΔG*, which governs the kinetic stability. Thermodynamic and kinetic stability can - but need not - be correlated (Ruiz-Sanchez, 2010). In fact, in SERT-TS3* there was a concomitant increase in thermodynamic and kinetic stability. In contrast, in SERT-P601A/G602A, the thermodynamic stability was reduced but the kinetic stability was not: it was actually modestly elevated (176 $kJ \cdot mol^{-1}$) relative to wild type SERT (113 $kJ \cdot mol^{-1}$). Divergent effects were also seen previously in adenosine A_1-receptor mutants (Nasrollahi-Shirazi et al., 2020). Similarly, cholesterol extraction also reduced thermodynamic stability but enhanced kinetic

Molecular Pharmacology Fast Forward. Published on December 5, 2021 as DOI: 10.1124/molpharm.121.000413
This article has not been copyedited and formatted. The final version may differ from this version.

stability. The membrane of the endoplasmic reticulum (ER) contains much less cholesterol than the plasma membrane. Folding of nascent membrane proteins must occur in the endoplasmic reticulum. Stabilizing effects of lipids introduce energy barriers in the folding trajectory and may thus impede the conformational search for the stable fold. The membrane of the ER differs from the plasmalemma by its substantially lower cholesterol content. We propose that this lower cholesterol content is a double-edged sword: it facilitates folding by reducing the energy difference between folding intermediates and the native state. The trade-off is that hydrophobic mismatch can introduce energy barriers, which are difficult to overcome. Under these conditions, point mutations, which impede folding, are more prone to stall the folding trajectory. This is exemplified by SERT-P601A/G602A: when pharmacochaperoned, SERT-P601A/G602A can overcome the conformational trap in the ER and reach the cell surface. There it is perfectly capable of sustaining the transport cycle, i.e. it can visit many conformations without any apparent rapid inactivation.

Authorship Contributions:

Participated in research design: Freissmuth, Koban, Stockner and Szöllősi

Conducted experiments: El-Kasaby, Ponleitner, and Szöllősi

Performed data analysis: El-Kasaby, Freissmuth, Koban, Ponleitner, Szöllősi and Stockner

Wrote or contributed to the writing of the manuscript: Freissmuth, Ponleitner, Stockner and Szöllősi.

Conflict of interest:

The authors declare no conflict of interest.

References:

Abraham MJ, Murtola T, Schulz R, Páll S, Smith JC, Hess B, and Lindahl E (2015) GROMACS: High performance molecular simulations through multi-level parallelism from laptops to supercomputers. *SoftwareX* **1-2**: 19-25.

Asjad HMM, Kasture A, El-Kasaby A, Sackel M, Hummel T, Freissmuth M, and Sucic S (2017) Pharmacochaperoning in a Drosophila model system rescues human dopamine transporter variants associated with infantile/juvenile parkinsonism. *J Biol Chem* **292**: 19250-19265.

Barducci A, Bussi G, and Parrinello M (2008) Well-tempered metadynamics: a smoothly converging and tunable free-energy method. *Phys Rev Lett* **100**: 020603.

Bhat S, Hasenhuetl PS, Kasture A, El-Kasaby A, Baumann MH, Blough BE, Sucic S, Sandtner W, and Freissmuth M (2017) Conformational state interactions provide clues to the pharmacochaperone potential of serotonin transporter partial substrates. *J Biol Chem* **292**: 16773-16786.

Bhat S, Newman AH, and Freissmuth M (2019) How to rescue misfolded SERT, DAT and NET: targeting conformational intermediates with atypical inhibitors and partial releasers. *Biochem Soc Trans* **47**: 861-874.

Bhat S, El-Kasaby A, Freissmuth M, and Sucic S (2021a) Functional and Biochemical consequences of disease variants in neurotransmitter transporters: a special emphasis on folding and frafficking deficits. Pharmacol. Ther. 222, 107785.

Bhat S, Niello M, Schicker K, Pifl C, Sitte HH, Freissmuth M, and Sandtner W (2021b) Handling of intracellular K+ determines voltage dependence of plasmalemmal monoamine transporter function. *Elife* **10**: e67996.

Bhat S, Guthrie DA, Kasture A, El-Kasaby A, Cao J, Bonifazi A, Ku T, Giancola, JB, Hummel T, Freissmuth M, and Newman AH (2021c) Tropane-based ibogaine analog rescues folding-deficient serotonin and dopamine transporters. *ACS Pharmacol Transl Sci* **4**: 503-516.

Bussi G, Donadio D, and Parrinello M (2007) Canonical sampling through velocity rescaling. J Chem Phys **126**: 014101.

César-Razquin A, Snijder B, Frappier-Brinton T, Isserlin R, Gyimesi G, Bai X, Reithmeier RA, Hepworth D, Hediger MA, Edwards AM, and Superti-Furga G (2015) A call for systematic research on solute carriers. *Cell* **162**: 478–487.

Coleman JA, Green EM, and Gouaux E (2016) X-ray structures and mechanism of the human serotonin transporter. *Nature* **532**: 334-339.

Coleman JA, and Gouaux E (2018) Structural basis for recognition of diverse antidepressants by the human serotonin transporter. *Nat Struct Mol Biol* **25**: 170-175.

Coleman JA, Yang D, Zhao Z, Wen PC, Yoshioka C, Tajkhorshid E, and Gouaux E (2019) Serotonin transporter-ibogaine complexes illuminate mechanisms of inhibition and transport. *Nature* **569**: 141-145.

Darden T, York D, and Pedersen L (1993) Particle mesh Ewald: An N· log(N) method for Ewald sums in large systems. *J Chem Phys* **98**: 10089-10092.

de Jong DH, Singh G, Bennett WF, Arnarez C, Wassenaar TA, Schäfer LV, Periole X, Tieleman, DP, and Marrink SJ (2013) Improved parameters for the Martini coarse-grained protein force field. *J Chem Theory Comput* **9**: 687-697.

Dill KA, and Chan HS (1997) From Levinthal to pathways to funnels. *Nat Struct Mol Biol* **4**: 10−19.

El-Kasaby A, Just H, Malle E, Stolt-Bergner PC, Sitte HH, Freissmuth M, and Kudlacek O (2010) Mutations in the carboxyl-terminal SEC24 binding motif of the serotonin transporter impair folding of the transporter. *J. Biol. Chem*. **285**: 39201-39210.

El-Kasaby A, Koban F, Sitte HH, Freissmuth M, and Sucic S (2014) A cytosolic relay of heat shock proteins HSP70-1A and HSP90β monitors the folding trajectory of the serotonin transporter. *J Biol Chem* **289**: 28987-29000.

El-Kasaby A, Kasture A, Koban F, Hotka M, Asjad HMM, Kubista H, Freissmuth M, and Sucic S (2019) Rescue by 4-phenylbutyrate of several misfolded creatine transporter-1 variants linked to the creatine transporter deficiency syndrome. *Neuropharmacology* **161**, 107572.

Esendir E, Burtscher V, Coleman JA, Zhu R, Gouaux E, Freissmuth M, Sandtner W. (2021) Extracellular loops of the serotonin transporter act as a selectivity filter for drug binding. *J. Biol. Chem*. **297**: 100863.

Fenollar-Ferrer C, Stockner T, Schwarz TC, Pal A, Gotovina J, Hofmaier T, Jayaraman K, Adhikary S, Kudlacek O, Mehdipour AR, Tavoulari S, Rudnick G, Singh SK, Konrat R, Sitte HH, and Forrest LR (2014) Structure and regulatory interactions of the cytoplasmic terminal domains of serotonin transporter. *Biochemistry* **53**: 5444–5460.

Ferraro M, Masetti M, Recanatini M, Cavalli A, and Bottegoni G (2016) Mapping cholesterol interaction sites on serotonin transporter through coarse-grained molecular dynamics. *PLoS One* **11**: e0166196.

Fogolari F, Maloku O, Dongmo Foumthuim CJ, Corazza A, and Esposito G (2018) PDB2ENTROPY and PDB2TRENT: Conformational and translational–rotational entropy from molecular ensembles. *J Chem Inf Model* **58**: 1319–1324.

Freissmuth M, Stockner T, and Sucic S (2017) SLC6 transporter folding diseases and pharmacochaperoning. *Handb Exp Pharmacol* **245**: 249−270.

Fujiwara M, Yamamoto H, Miyagi T, Seki T, Tanaka S, Hide I, Sakai N (2013) Effects of the chemical chaperone 4-phenylbutylate on the function of the serotonin transporter (SERT) expressed in COS-7 cells. *J Pharmacol Sci* **122**: 71-83.

Green EM, Coleman JA, and Gouaux E (2015) Thermostabilization of the human serotonin transporter in an antidepressant-bound conformation. *PLoS One* **10**: e0145688.

Hartl FU, Bracher A, Hayer-Hartl M (2011) Molecular chaperones in protein folding and proteostasis. *Nature* **475**: 324-332.

Hasenhuetl PS, Freissmuth M, and Sandtner W (2016) Electrogenic binding of intracellular cations defines a kinetic decision point in the transport cycle of the human serotonin transporter. *J Biol Chem* **291**: 25864-25876.

Hasenhuetl PS, Bhat S, Freissmuth M, and Sandtner W (2019) Functional selectivity and partial efficacy at the monoamine transporters: a unified model of allosteric modulation and amphetamine-induced substrate release. *Mol Pharmacol* **95**: 303-312.

Jämbeck JP, and Lyubartsev AP (2012) An extension and further validation of an all-atomistic force field for biological membranes. *J Chem Theory Comput* **8**: 2938-2948.

Jämbeck JP, and Lyubartsev AP (2013) Another piece of the membrane puzzle: extending Slipids further. *J Chem Theory Comput* **9**: 774-784.

Jones KT, Zhen J, and Reith M (2012) Importance of cholesterol in dopamine transporter function. *J Neurochem* **123**: 700-715.

Karshikoff A, Nilsson L, and Ladenstein R (2015) Rigidity versus flexibility: the dilemma of understanding protein thermal stability. *FEBS J* **282**: 3899–3917.

Kasture A, El-Kasaby A, Szöllősi D, Asjad HMM, Grimm A, Stockner T, Hummel T, Freissmuth M, and Sucic S (2016) Functional rescue of a misfolded Drosophila melanogaster dopamine transporter mutant associated with a sleepless phenotype by pharmacological chaperones. *J Biol Chem* **291**: 20876-20890.

Koban F, El-Kasaby A, Häusler C, Stockner T, Simbrunner BM, Sitte HH, Freissmuth M, and Sucic S (2015) A salt bridge linking the first intracellular loop with the C terminus facilitates the folding of the serotonin transporter. *J Biol Chem* **290**: 13263-13278.

Laursen L, Severinsen K, Kristensen KB, Periole X, Overby M, Müller HK, Schiøtt B, and Sinning S (2018) Cholesterol binding to a conserved site modulates the conformation, pharmacology, and transport kinetics of the human serotonin transporter. *J Biol Chem* **293**: 3510-3523.

Marinko JT, Huang H, Penn WD, Capra JA, Schlebach, JP, and Sanders CR (2019) Folding and misfolding of human membrane proteins in health and disease: from single molecules to cellular proteostasis. *Chem Rev* **119**: 5537−5606.

Lindahl V, Villa A, and Hess B (2017) Sequence dependency of canonical base pair opening in the DNA double helix. *PLoS Comput Biol* **13**: e1005463.

Lindorff-Larsen K, Piana S, Palmo K, Maragakis P, Klepeis JL, Dror RO, and Shaw DE (2010) Improved side-chain torsion potentials for the Amber ff99SB protein force field. *Proteins* **78**: 1950-1958.

Lumry R, and Eyring H (1954) Conformation Changes of Proteins. *J Phys Chem.* **58**: 110–120.

Maneri LR, and Low PS (1988) Structural stability of the erythrocyte anion transporter, band 3, in different lipid environments. A differential scanning calorimetric study. *J Biol Chem* **263**: 16170–16178.

Monticelli L, Kandasamy SK, Periole X, Larson RG, Tieleman, DP, and Marrink SJ (2008) The MARTINI coarse-grained force field: extension to proteins. *J Chem Theory Comput* **4**: 819-834.

Nasrollahi-Shirazi S, Szöllősi D, Yang Q, Muratspahic E, El-Kasaby A, Sucic S, Stockner T, Nanoff C, and Freissmuth M (2020) Functional Impact of the G279S substitution in the adenosine A1-receptor (A1R-G279S$^{7.44}$), a mutation associated with Parkinson's disease. *Mol Pharmacol* **98**: 250-266.

Parinello M, and Rahman A (1981) Polymorphic transitions in single crystals: A new molecular dynamics method. *J Appl Phys* **52**: 7182-7190.

Penmatsa A, Wang KH, and Gouaux E (2013) X-ray structure of dopamine transporter elucidates antidepressant mechanism. *Nature* **503**: 85-90.

Perland E, and Fredriksson R. (2017) Classification systems of secondary active transporters. *Trends Pharmacol Sci* **38**: 305–315.

The PLUMED consortium (2019) Promoting transparency and reproducibility in enhanced molecular simulations. *Nat Methods* **16**: 670–673.

Sanchez-Ruiz JM (2010) Protein kinetic stability. *Biophys. Chem.* **148**: 1–15.

Scanlon SM, Williams DC, and Schloss P. (2001) Membrane cholesterol modulates serotonin transporter activity. *Biochemistry* **40**: 10507–10513.

Schaller L, and Lauschke VM (2019) The genetic landscape of the human solute carrier (SLC) transporter superfamily. *Hum. Genet.* **138**: 1359–1377.

Schicker K, Uzelac Z, Gesmonde J, Bulling S, Stockner T, Freissmuth M, Boehm S, Rudnick G, Sitte HH, and Sandtner W (2012) Unifying concept of serotonin transporter-associated currents. *J Biol Chem* **287**: 438-445.

Shen MY, and Sali A (2006) Statistical potential for assessment and prediction of protein structures. *Protein Sci* **15**: 2507-2524.

Shouffani A, and Kanner BI (1990) Cholesterol is required for the reconstruction of the sodium- and chloride-coupled, gamma-aminobutyric acid transporter from rat brain. *J Biol Chem* **265**: 6002–6008.

Sitte HH, and Freissmuth M (2015) Amphetamines, new psychoactive drugs and the monoamine transporter cycle. *Trends Pharmacol Sci* **36**: 41-50.

Tate CG, Haase J, Baker C, Boorsma M, Magnani F, Vallis Y, and Williams DC (2003) Comparison of seven different heterologous protein expression systems for the production of the serotonin transporter. *Biochim Biophys Acta* **1610**: 141-153.

Tiwary P, and Parrinello M (2015) A time-independent free energy estimator for metadynamics. *J Phys Chem B* **119**: 736–742.

Tribello, G.A., Bonomi, M., Branduardi, D., Camilloni, C., and Bussi G. (2014) PLUMED 2: New feathers for an old bird. *Computer Physics Communications* **185**, 604-613.

Tsien RY (1998) The green fluorescent protein. *Annu Rev Biochem.* **67**: 509–544.

Wassenaar TA, Ingólfsson HI, Böckmann RA, Tieleman DP, and Marrink SJ (2015) Computational lipidomics with insane: a versatile tool for generating custom membranes for molecular simulations. *J Chem Theory Comput* **11**: 2144-2155.

Wassenaar TA, Pluhackova K, Böckmann RA, Marrink SJ, and Tieleman DP (2014) Going backward: a flexible geometric approach to reverse transformation from coarse grained to atomistic models. *J Chem Theory Comput* **10**: 676-690.

Webb B, and Sali A (2014) Protein structure modeling with MODELLER. *Methods Mol Biol* **1137**: 1-15.

Wolf MG, Hoefling M, Aponte-Santamaría C, Grubmüller H, and Groenhof G (2010) g_membed: efficient insertion of a membrane protein into an equilibrated lipid bilayer with minimal perturbation. *J Comput Chem* **31**: 2169-2174.

Footnotes:

This work was supported by a grant from the Vienna Science and Technology Fund/WWTF (LSC17-026 to M.F.) and from the Austrian Science fund/FWF (P 32017 to T.S.). The simulations were performed using the resources of the Vienna Scientific Cluster (VSC).

* M.P. and D. S. contributed equally.

Molecular Pharmacology Fast Forward. Published on December 5, 2021 as DOI: 10.1124/molpharm.121.000413
This article has not been copyedited and formatted. The final version may differ from this version.

Figure legends

Figure 1. Thermostability of SERT-wt, SERT-TS_2^*, SERT-TS_3^* and SERT-P601A/G602A. Melting curves of stably expressed transporter variants, i.e. wild type SERT (SERT-wt, circles), SERT-I291A/ T439S (TS_2^*, triangles), SERT-$Y^{110}A/I^{291}A/ T^{439}S$ (TS_3^*, squares) **SERT-P601A/G602A** (SERT-PG, triangles). Membranes prepared from HEK293 cells stably expressing transporter variants (5 to 40 µg/assay) were incubated for 15 min at the indicated temperatures; membranes harboring wild type SERT were also incubated in buffer, where Na^+ was replaced by equimolar choline (empty circles). Samples were placed on ice and [^{3}H]imipramine was added to give a final concentration of 3 nM. After an incubation of 15 min on ice the reaction was terminated by rapid filtration. Data were normalized to control specific binding (i.e. binding determined at 22°C in the absence of thermal denaturation represents 100%); this binding was 94.8 ± 10.7, 17.9 ± 2.2, 18.9 ± 7.1 and 18.3 ± 1.3 fmol/assay for wild type SERT, SERT-TS2*, SERT-TS3* and SERT-P601A/G602A, respectively. Data are the means ± S.D. from at least three different experiments carried out in duplicate. The solid curves were drawn by fitting the data to the three-parameter logistic equation.

Fig. 2. Structural and dynamic effect of stabilizing mutations. A) The three thermostabilizing mutations Y110A, I291A and T439S are highlighted in van der Waals rendering. The mobility of residues observed in the simulations is reflected by the thickness of the ribbon representation of the structure of SERT. B) Average per residue root mean square fluctuations (RMSF) of wild type SERT (WT, blue) and SERT-TS3 (TS3, red). The last 250 ns with 1 ns time resolution of each trajectory were used for the analysis. The positions of the mutated residues in the primary sequence of SERT are indicated by vertical dashed lines. The location of transmembrane helices 1-12 and of extracellular loops 2-4 is indicated by yellow and orange boxes, respectively. C) Comparison of representative conformations of TM1, TM6

and EL4 of SERT (WT, blue) and SERT-TS3 (TS3, red). The structures are fitted onto the scaffold domain (TM3, TM4, TM8, TM9). D) Distance between TM1b (center of Cα atoms residue 99-111) and TM9 (center of Cα atoms residue 475-477) as a measure for occlusion. The last 250 ns of each trajectory with 1 ns time resolution were used as input data. E) The number of residues (Cα positions) within 1 nm of the Cα position of residue 110 indicates that the Y110A mutant increase local packing. The last 250 ns of each trajectory with 10 ns time resolution were used as input data. F) Sub-atom size void (larger than 0.05 nm) next to residue 291. Empty regions are highlighted by cyan for wild type SERT (blue) and by magenta for SERT-TS3 (red). The last 250 ns with 1 ns time resolution of each trajectory were used as input data and averaged over independent trajectories. The same representative structures were used as in panel C. G) Distance between the Cα atoms of residue 291 (TM5) and I426 (TM8), shown as orange line in panel F, indicates changes in transmembrane helix packing. The last 250 ns of each trajectory with 1 ns time resolution were used as input data. H) Distribution of the χ1 angle of I426. The last 250 ns of each trajectory with 0.1 ns time resolution were used as input data. I) Water density is shown in blue next to residue T439 in wild type SERT or J) SERT-TS3. Bulk water density is 1000 kg/m^3. The last 250 ns of each trajectory with 0.1 ns time resolution were used as input data and averaged over all trajectories. K) The distance between the hydroxyl group of T439 (WT, blue) or S439 (TS3, red) and the backbone oxygen of G435 or L) the amino group of N177 indicates changes in the local hydrogen bonding pattern. The respective distances are indicated by orange lines on panel I and J. The last 250 ns of each trajectory with 1 ns time resolution were used as input data.

Fig. 3. Effect of the SERT-P601A/G602A mutation on protein dynamics and on the attachment of the C-terminus to the protein core. A) Overview image showing the mutation PG601,602AA (red van der Waals rendering) and the reaction coordinate used for

the biased simulations defined as the distance (dashed red line) between the centers of mass of TM12 (blue) and the C-terminal helix (grey). Distances between Cα of P156-S611 and L597-R607 are indicated by orange and cyan lines, respectively. B) Average per residue root mean square fluctuations (RMSF) of wild type SERT (WT, blue; same as in Fig. 2B) and SERT-PG601,602AA (PG, green). The location of transmembrane helices 1-12 and of extracellular loops 1-4 is indicated by yellow and orange boxes, respectively. C) A close-up of RMSF to the TM12 - C-terminal segment of the protein. The positions of the mutated residues in the primary sequence of SERT are indicated by vertical dashed lines. The last 250 ns with 1 ns time resolution of each trajectory were used for the analysis. D) Free energy landscape calculated by well-tempered metadynamics method showing wild type SERT on the left and SERT-P601A/G602A on the right.

Figure 4. Time-dependent thermal inactivation of wild type SERT, SERT-TS$_3$* and SERT-P601A/G602A. The assay was carried out with membranes prepared from HEK293 cells stably expressing wild type SERT (*A*, SERT-wt), SERT-TS3*(*B*) and SERT-P601A/G602A (*C*, SERT-PG), which were incubated at the indicated temperatures for the indicated time periods. Thereafter, the samples were placed on ice and [^{3}H]imipramine was added to reach a final concentration of 3 nM. The binding reaction was carried out on ice as outlined under Materials and Methods. Data were normalized to control specific binding (i.e. binding determined in the absence of thermal denaturation represents 100%, see Fig. 1) and represent the means ± S.D. from three independent experiments. The lines were drawn by fitting the data to the equation for a mono- or double-exponential decay; the equation for a monoexponential decay gave an adequate description for the curves at the highest temperature (green line). In the three other instances (blue and violet lines), the double-exponential decay significantly improved the fit ($p<0.05$, F-test based on the extra-sum of square principle).

Molecular Pharmacology Fast Forward. Published on December 5, 2021 as DOI: 10.1124/molpharm.121.000413
This article has not been copyedited and formatted. The final version may differ from this version.

Figure 5. Arrhenius plots for the slow (A) and the fast rate of heat inactivation (B) and the ratio of folded to unfolded protein *Pf/Pu (C)*. The rates of rapid and slow inactivation were taken from the curves shown in Fig. 4. Note that the rates of the fast component are only shown for those instances, where their calculation was anchored by an adequate number of points (see Fig. 4). The values for *Pf/Pu* were also calculated from the biexponential fit and thus limited to temperatures below and around T_M. Error bars represent the standard error of the parameters extracted from the fitting procedure. The lines were drawn using linear regression.

Figure 6. Membrane protein interaction in membranes containing solely POPC or a mixture of cholesterol and POPC. A) Side view of membrane-embedded wild type SERT. The phosphate atoms of POPC are highlighted as colored spheres (red, membranes containing only POPC; blue, membranes containing cholesterol and POPC) to indicate the location of the head groups in the last 100 ns of a representative simulation. **B)** Mean membrane thickness measured in relation to the distance from the center of the protein: membrane thickness was averaged over points equidistant from the protein center, i.e. the radial average was plotted. The thickness was measured between the phosphate atoms of the head groups in the inner and outer leaflet. Each line represents a complete simulation with 10 ps time resolution of conformation sampling. **C-D)** Map of membrane thickness viewed from the extracellular side. SERT cartoon representation indicates the protein orientation with the C-terminal helix highlighted in black. The black and orange arrow in C point to local thinning of the membrane in the vicinity of TM2 and TM5, respectively. The magenta arrow in D highlights membrane thickening in the vicinity of TM11.

Fig. 7. Effect of cholesterol removal on the local mobility of residues in wild type SERT. A&C: Average per residue root mean square fluctuations (RMSF) for Cα (A) or side chains

(B) of wild type SERT embedded in a bilayer containing (blue) or lacking cholesterol (light blue). The entire trajectories (i.e. 500 ns simulation with 1 ns time resolution) were used for the analysis. The location of transmembrane helices 1-12, of extracellular loops 2-4 of intracellular loop 4 are indicated by yellow, orange and green boxes, respectively. B&D: Difference in per residue RMSF for Cα (B) or individual side chains (D) resulting from subtraction of the data shown in A and D, respectively. The red lines highlight the averaged differences over the sequence elements (i.e. TM1-12, EL2-4 and IL4) indicated by the colored boxes.

Figure 8. Effect of cholesterol depletion on the melting curve of wild type SERT (A) and SERT-V367N (B) and time-dependent thermal inactivation of wild type SERT after cholesterol depletion (C-E). Binding assays were performed on membranes prepared from HEK293 cells stably expressing wild type SERT (A, SERT-wt) or SERT-V367N (B, SERT-VN). Cholesterol was depleted by incubating membranes for 30 min at 37°C in the presence of 10 mg/ml methyl-β-cyclodextrin (MBCD, open circles). Control samples were subjected to a similar preincubation in the absence of MBCD (black circles). C) Membranes from HEK293 cells stably expressing wild type SERT were extracted with MBCD as in panel A and incubated at the indicated temperatures for the indicated time periods. Thereafter, the binding reaction was carried out on ice as outlined under Materials and Methods. The rates of slow inactivation (D) and the ratio of slowly to rapidly unfolding (P_f/P_u, panel E) were estimated by fitting the data in panel C to the equation for a double exponential decay. Data were normalized to control [^{3}H]imipramine binding in the absence of thermal denaturation (=100%) and represent the average of five (A,B) and three (C-E) independent experiments carried out in duplicates. Error bars represent S.D. (A-C) or the standard error of the parameter (D,E). Lines were drawn by fitting the data to the three-parameter logistic equation (A,B), to the equation for a double-exponential decay (C) or by linear regression (D,E).

Figure 1

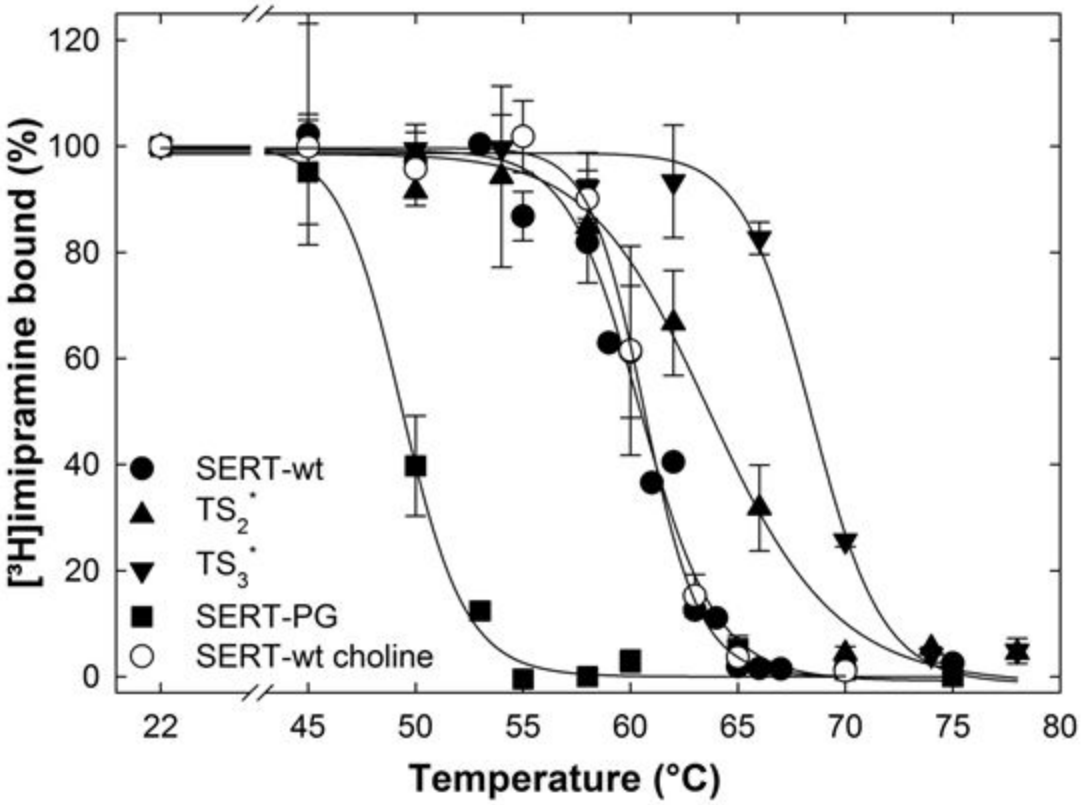
[³H]imipramine bound (%)
120
100
80
60
40
20
0
22
45
50
55
60
65
70
75
80
Temperature (°C)
SERT-wt
TS2*
TS3*
SERT-PG
SERT-wt choline

Figure 2

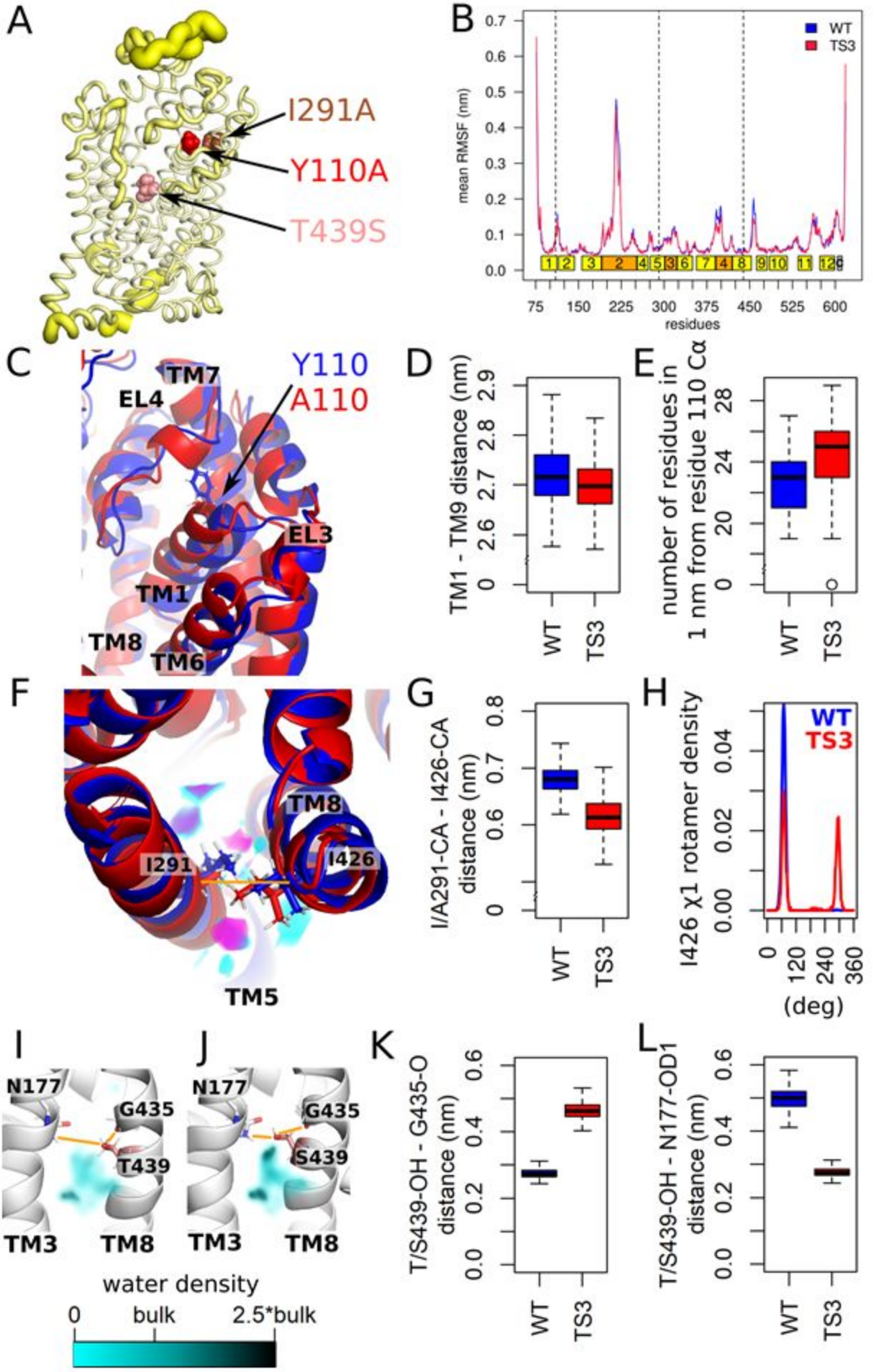
A
I291A
Y110A
T439S
B
WT
TS3
mean RMSF (nm)
residues
C
TM7
EL4
Y110
A110
EL3
TM1
TM8
TM6
D
TM1 - TM9 distance (nm)
WT
TS3
E
number of residues in
1 nm from residue 110 Cα
F
TM8
I291
I426
TM5
G
I/A291-CA - I426-CA
distance (nm)
H
I426 χ1 rotamer density
(deg)
I
N177
G435
T439
TM3
TM8
J
N177
G435
S439
TM3
TM8
water density
0
bulk
2.5*bulk
K
T/S439-OH - G435-O
distance (nm)
L
T/S439-OH - N177-OD1
distance (nm)

Figure 3

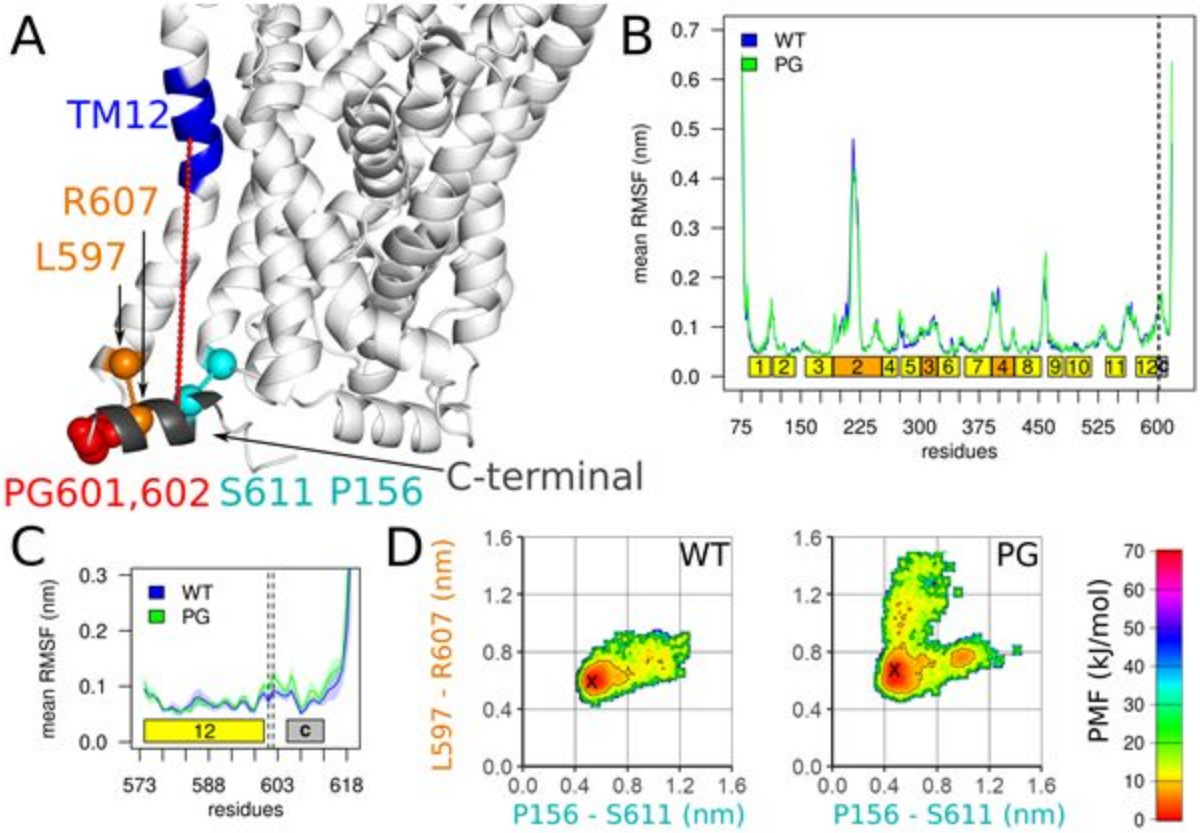
A
TM12
R607
L597
PG601,602
S611
P156
C-terminal
B
WT
PG
mean RMSF (nm)
residues
C
WT
PG
mean RMSF (nm)
residues
D
WT
PG
L597 - R607 (nm)
P156 - S611 (nm)
PMF (kJ/mol)

Figure 4

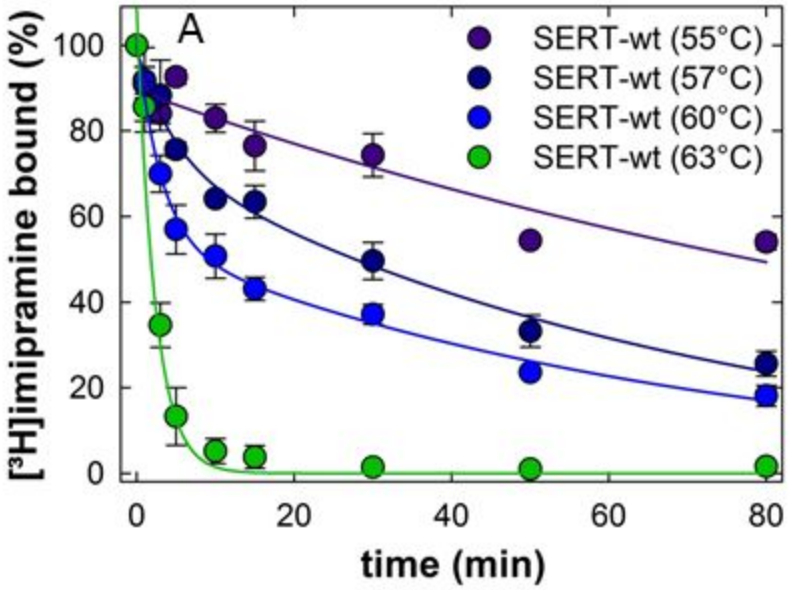
A
SERT-wt (55°C)
SERT-wt (57°C)
SERT-wt (60°C)
SERT-wt (63°C)
[³H]imipramine bound (%)
time (min)

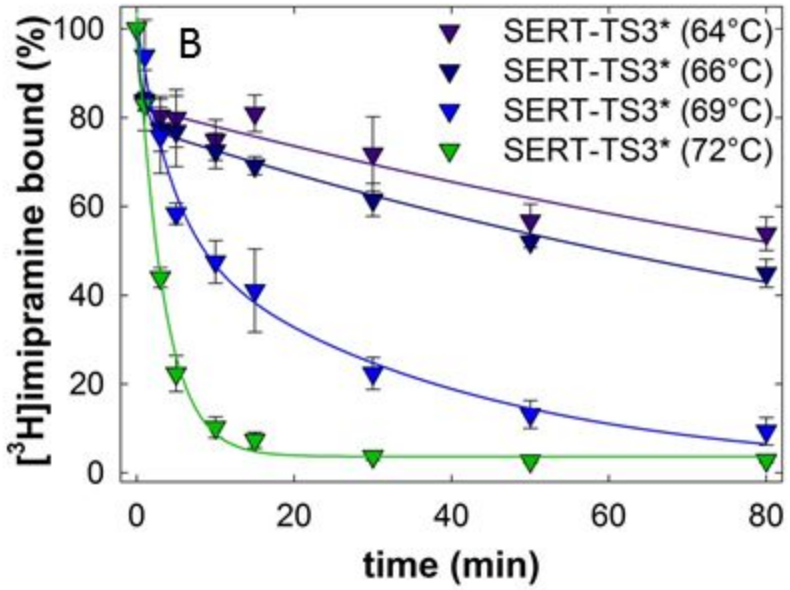
B
SERT-TS3* (64°C)
SERT-TS3* (66°C)
SERT-TS3* (69°C)
SERT-TS3* (72°C)
[³H]imipramine bound (%)
time (min)

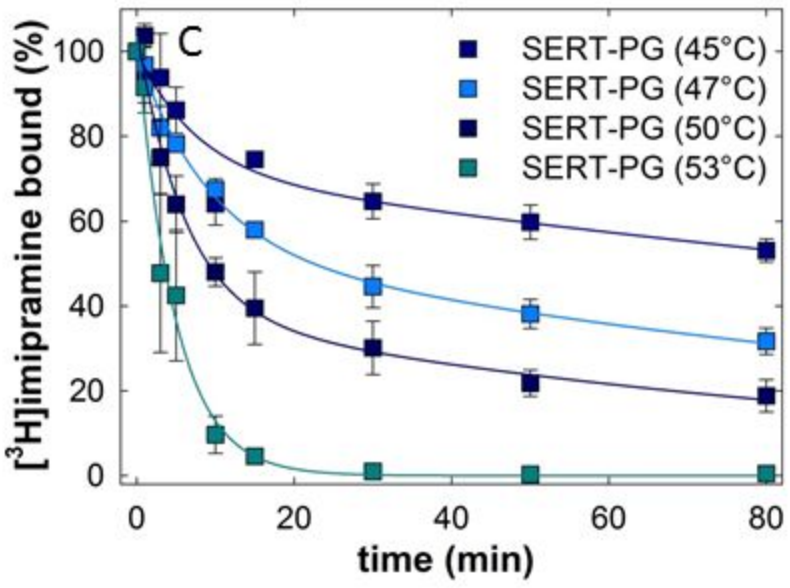
C
SERT-PG (45°C)
SERT-PG (47°C)
SERT-PG (50°C)
SERT-PG (53°C)
[³H]imipramine bound (%)
time (min)

Figure 5

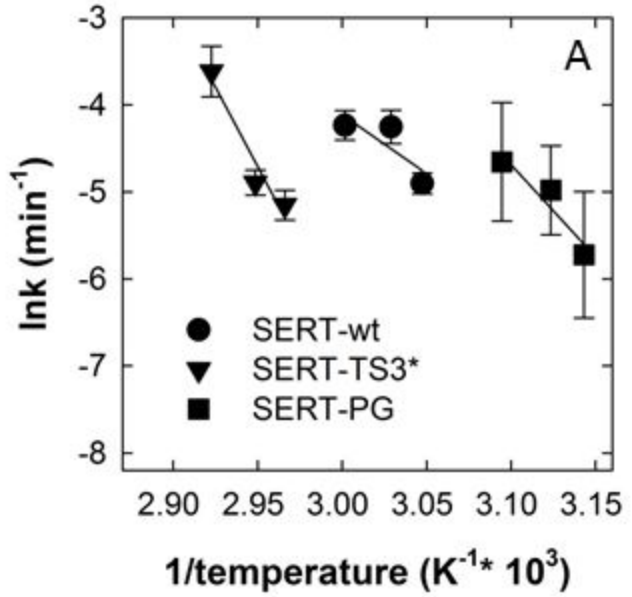
A
lnk (min-1)
-3
-4
-5
-6
-7
-8
SERT-wt
SERT-TS3*
SERT-PG
2.90 2.95 3.00 3.05 3.10 3.15
1/temperature (K-1* 10^3)

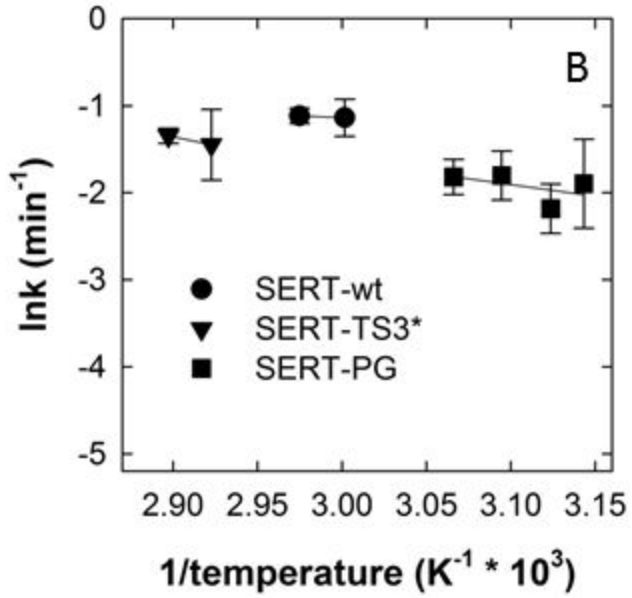
B
lnk (min-1)
0
-1
-2
-3
-4
-5
SERT-wt
SERT-TS3*
SERT-PG
2.90 2.95 3.00 3.05 3.10 3.15
1/temperature (K-1 * 10^3)

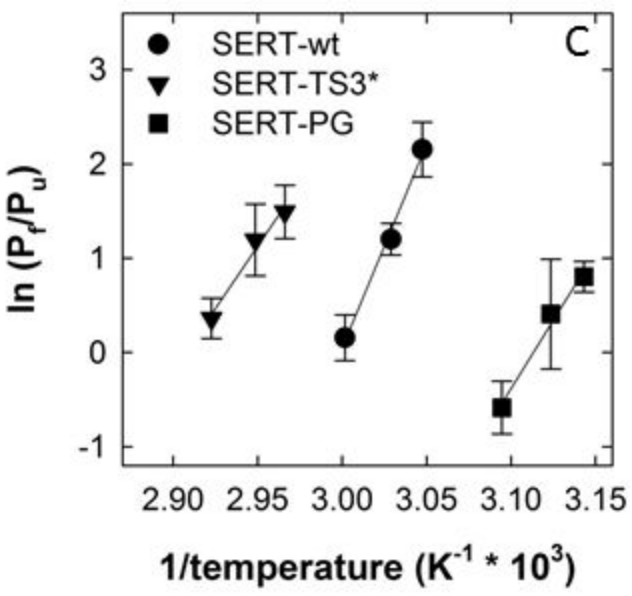
C
SERT-wt
SERT-TS3*
SERT-PG
ln (Pf/Pu)
3
2
1
0
-1
2.90 2.95 3.00 3.05 3.10 3.15
1/temperature (K-1 * 10^3)

Figure 6

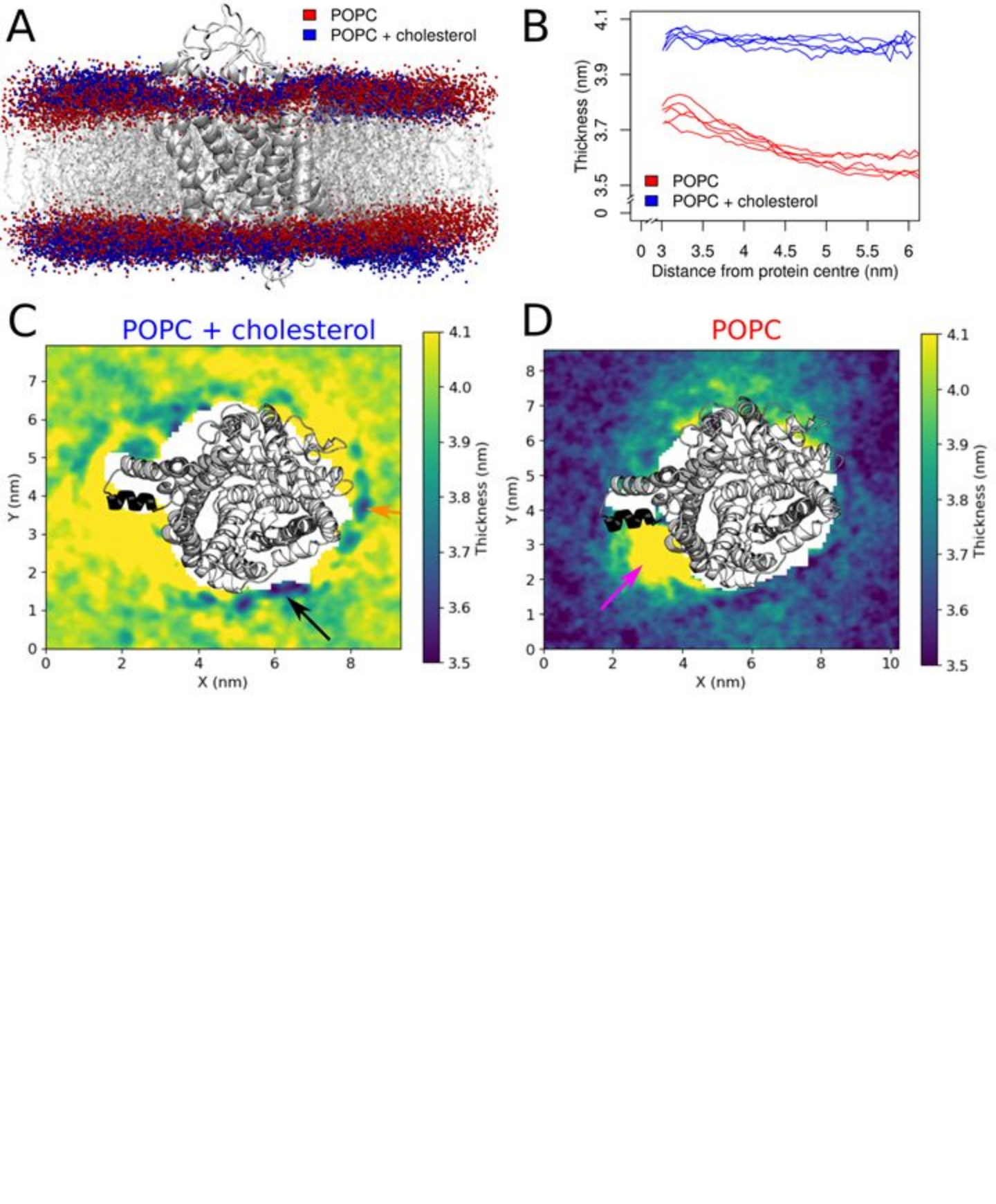
A
POPC
POPC + cholesterol
B
Thickness (nm)
0 3.5 3.7 3.9 4.1
POPC
POPC + cholesterol
0 3 3.5 4 4.5 5 5.5 6
Distance from protein centre (nm)
C
POPC + cholesterol
Y (nm)
X (nm)
Thickness (nm)
4.1 4.0 3.9 3.8 3.7 3.6 3.5
D
POPC
Y (nm)
X (nm)
Thickness (nm)
4.1 4.0 3.9 3.8 3.7 3.6 3.5

Figure 7

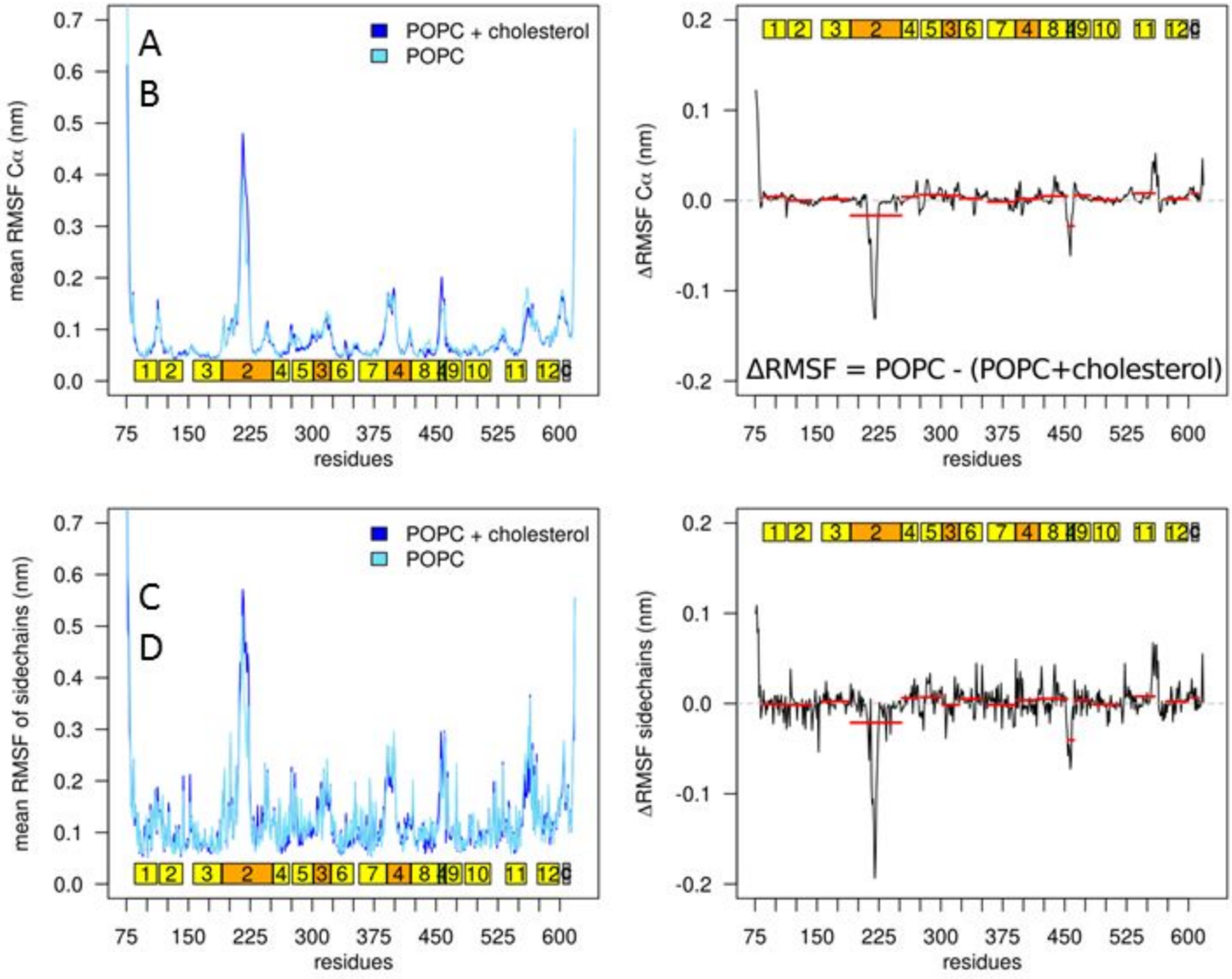
A
B
POPC + cholesterol
POPC
mean RMSF Cα (nm)
ΔRMSF Cα (nm)
ΔRMSF = POPC - (POPC+cholesterol)
C
D
mean RMSF of sidechains (nm)
ΔRMSF sidechains (nm)
residues

Figure 8

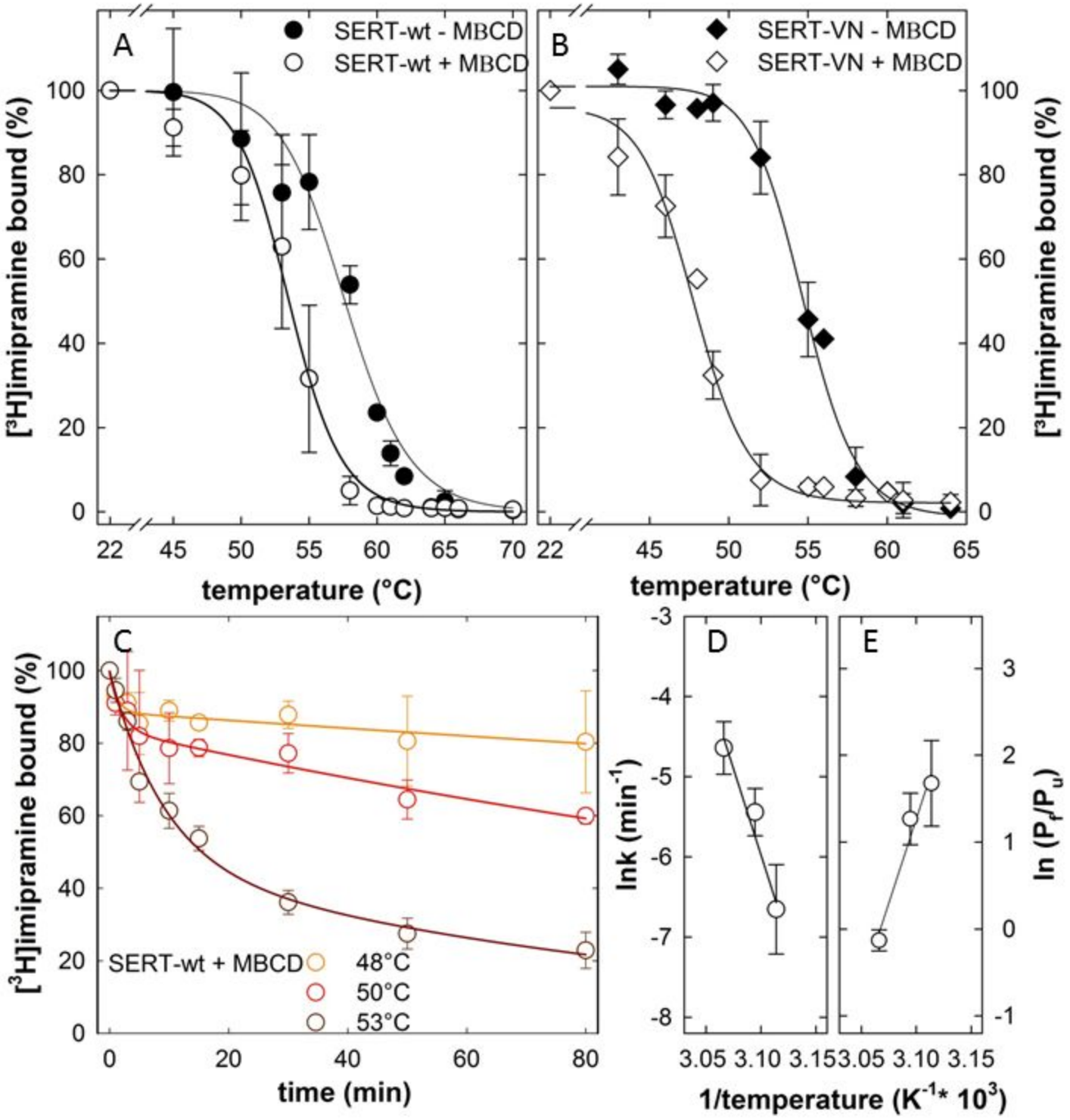
A
SERT-wt - MBCD
SERT-wt + MBCD
[³H]imipramine bound (%)
temperature (°C)
B
SERT-VN - MBCD
SERT-VN + MBCD
[³H]imipramine bound (%)
temperature (°C)
C
[³H]imipramine bound (%)
SERT-wt + MBCD
48°C
50°C
53°C
time (min)
D
lnk (min⁻¹)
1/temperature (K⁻¹* 10³)
E
ln (Pf/Pu)
1/temperature (K⁻¹* 10³)